frontiers in Physics

ORIGINAL RESEARCH
published: 10 January 2020
doi: 10.3389/fphy.2019.00224

Diffusion of Anisotropic Particles in Random Energy Landscapes—An Experimental Study

Juan Pablo Segovia-Gutiérrez[1], *Manuel A. Escobedo-Sánchez*[1], *Erick Sarmiento-Gómez*[1,2] *and Stefan U. Egelhaaf*[1]*

[1] Condensed Matter Physics Laboratory, Heinrich Heine University, Düsseldorf, Germany, [2] División de Ciencias e Ingenierías, Departamento de Ingeniería Física, Universidad de Guanajuato, León, Mexico

If a colloidal particle is exposed to an external field, its Brownian motion is modified. In the case of an anisotropic particle, the external potential might not only affect its translation but also its rotation. We experimentally investigate the dynamics of a trimer, which consists of three spherical particles, within a random potential energy landscape. This energy landscape has energy values drawn from a Gamma distribution, a spatial correlation length similar to the particle size and is realized by a random light field, that is a laser speckle pattern. The particle translation and rotation are quantified by the mean squared (angular) displacement, the van Hove function and other observable quantities. The translation shows an intermediate subdiffusive regime and a long-time diffusion that slows down upon increasing the modulation of the potential. In contrast, the mean squared angular displacement exhibits only small deviations from a linear time dependence but a more detailed analysis reveals discrete angular jumps reflecting the symmetry of the trimer. A coupling between the translation and rotation is observed and found to depend on the length scale.

Keywords: random walk, anomalous diffusion, translational motion, rotational motion, potential energy landscape, colloidal molecules, video microscopy

OPEN ACCESS

Edited by:
Ralf Metzler,
University of Potsdam, Germany

Reviewed by:
Heiko Rieger,
Saarland University, Germany
Andrew James Spakowitz,
Stanford University, United States

***Correspondence:**
Stefan U. Egelhaaf
stefan.egelhaaf@uni-duesseldorf.de

Specialty section:
This article was submitted to Interdisciplinary Physics, a section of the journal Frontiers in Physics

Received: *08 August 2019*
Accepted: *02 December 2019*
Published: *10 January 2020*

Citation:
Segovia-Gutiérrez JP, Escobedo-Sánchez MA, Sarmiento-Gómez E and Egelhaaf SU (2020) Diffusion of Anisotropic Particles in Random Energy Landscapes—An Experimental Study. Front. Phys. 7:224. doi: 10.3389/fphy.2019.00224

1. INTRODUCTION

Colloidal particles undergo random thermal motion. Free diffusion is characterized by a mean squared displacement which increases linearly with time. The slope is determined by the diffusion coefficient that depends on the temperature, the particle size, and the viscosity of the medium. However, colloidal particles in more complex situations, for example in the presence of interparticle interactions or external potentials, can show different behavior such as subdiffusion or superdiffusion. These imply mean squared displacements with time dependencies that are less than or greater than linear, respectively [1]. Such dynamics are frequently encountered in systems with biological or industrial relevance. For example, they are observed in living cells [2–5], biological membranes [6–8], porous media [9], and glassy systems [10–14]. Due to the analogy between the behaviors of colloidal particles and many different complex and experimentally less accessible systems, colloidal suspensions are frequently used as model systems to systematically and quantitatively study particle dynamics.

Although spherical colloidal particles are usually investigated, most molecular, biological or industrial systems contain non-spherical objects. The behavior of these objects can be modeled using anisotropic colloidal particles, which can be made using different synthesis routes [15–18]. Anisotropy introduces additional degrees of freedom but also, for instance,

more complex interparticle interactions and particle dynamics. Anisotropic particles are, therefore, also interesting in their own right. For example, elongated particles, such as ellipsoidal particles and dumbbells made of two spherical particles, show free diffusion that, up to intermediate times, shows a directional dependence [19, 20]. In addition, experiments on dumbbells and planar clusters of colloidal particles have shown a decoupling between translational and rotational motion at high concentrations [21, 22]. A more complex system, tetrahedral colloidal clusters immersed in a supercooled colloidal fluid, was investigated [23]. Also in this system a decoupling between translational and rotational diffusion was observed when the volume fraction approached the glass transition. Furthermore, molecular dynamics simulations revealed that dumbbells in a porous medium show dynamical heterogeneities [24]. This illustrates that an anisotropic shape as well as external constraints can significantly change the particle dynamics.

Colloidal particles can be manipulated using optical trapping, a phenomenon exploited in optical tweezers [25, 26]. Optical trapping relies on the momentum transfer between the photons to the colloidal particles during refraction and scattering. The magnitude of the effect depends on the intensity and intensity gradient of the light, the refractive index mismatch between the medium and the particle, the wavelength of the light and the particle size and shape [27–29]. In addition to optical tweezers, extended light fields can be used to expose particles to external potential energy landscapes [30]. Different light fields can be created to produce random, periodic or other potential energy landscapes [31–36]. Typically, energy modulations of the order of the thermal energy, k_BT, are applied. Subjecting colloids to these energy landscapes will affect their dynamics [30, 37–41]. Therefore, colloids exposed to light fields can serve as a model system to investigate the effect of external potentials on the particle dynamics.

Recently light fields have also been imposed on anisotropic particles [36, 42, 43]. Dilute suspensions of ellipsoids or multimers consisting of spherical particles, particularly dimers and trimers, have been subjected to a periodic light field. In the case of multimers, this results in a small number of preferred states, which reflects the limited number of spatial and orientational configurations the multimers attain due to their confinement in the periodic energy minima. The actual number of configurations depends on the ratio between the particle size and the periodicity of the potential. This suggests that the translational and rotational motions are coupled.

In this work, we study the translational and rotational dynamics of trimers. Trimers are anisotropic particles consisting of three spherical colloidal particles bonded together. They are exposed to a random light field, which imposes a random potential energy landscape. Due to the convolution of the light field with the particle volume, the distribution of energy values follows a Gamma distribution and the spatial correlation length of the potential is about the size of an individual sphere [34]. We characterize the dynamics by several parameters, such as the mean squared (angular) displacement and the van Hove function. The random potential energy landscape leads to an intermediate subdiffusive regime in the translational motion and the long-time translational diffusion is found to be reduced upon increasing the modulation of the potential, which is controlled by the laser intensity. The mean squared angular displacement, however, is hardly affected by the external potential. Nevertheless, a detailed quantitative analysis of the rotational motion uncovers characteristic angular jumps of approximately 120° that reflect the three-fold symmetry of the trimers. Furthermore, it reveals a complex coupling between the translational motion and the rotational motion.

2. MATERIALS AND METHODS

2.1. Synthesis of Trimers and Sample Preparation

Cross-linked poly(methyl methacrylate) (PMMA) spheres with a diameter $\sigma \approx 2.1$ μm were synthesized based on previously established methods [44–46]. After the synthesis, the solvent was exchanged by centrifugation in a two-step washing process: first, the suspension was washed three times with n-hexane (Sigma-Aldrich, Ref. Num. 1043671000) to remove leftovers from the reaction, then seven times with decahydronaphthalene (mixture of cis and trans isomers, 98%, Alfa Aesar, Ref. Num. A13883) to change the solvent to decahydronaphthalene. The particle suspension at 30 vol% was then used as stock to prepare trimers [18]. First, decahydronaphthalene was replaced with toluene (anhydrous, 99.8%, Sigma-Aldrich, Ref. Num. 244511) by washing three times. After the last washing step a suspension with a volume fraction of 3.66 vol% was obtained. 3 ml of this suspension was mixed with 15 ml of ultra pure water (resistivity 18 MΩ/cm) containing 0.5 wt% sodium dodecyl sulfate (SDS, Sigma-Aldirch, Ref. Num. L4509) to yield the precursor emulsion. To narrow down the size distribution of the emulsion droplets, the emulsion was homogenized by applying a T25 ULTRA-TURRAX® (IKA, Ref. Num. IK0003725000) for 60 s at 8,000 rpm followed by 25 s at 9,600 rpm. The emulsion was poured into a round-bottomed reaction flask with a capacity of 100 ml and subsequently placed in a constant temperature bath at 80 °C. The sample was slowly stirred for 2 h while the toluene evaporated.

The obtained suspension contained different multimers. It was, therefore, fractionated using a density gradient from a water-saccharose-surfactant solution. The density gradient was prepared from two solutions. The denser solution (density $\rho \approx$ 1.17 g/ml) contained 40 wt% D(+)-Saccharose (99.5%, Sigma-Aldrich, Ref. Num. 4661.1) and 0.1 wt% SDS. The less dense solution ($\rho \approx$ 1.08 g/ml) was prepared by diluting the denser solution by a factor of two with ultra pure water; typically 5 ml of the denser solution was diluted with 5 ml of water. Equal volumes of the two solutions were mixed using a density gradient maker with two chambers where each chamber was filled with one of the solutions. The mixed solution was transferred into a round-bottomed glass centrifuge tube. Then, the suspension containing the clusters was carefully loaded on top of the gradient column yielding a thin layer with a height of about 0.5 cm. The tube subsequently was placed in a centrifuge (Hermle Z323, rotor 221.12V01) and subjected to 2,000 rpm centrifugation for

4 min with the brake set to 0. This procedure was repeated many times to obtain a sufficient amount of trimer suspension. Finally, the collected suspension was washed a few times with ultra pure water to remove the surfactant and saccharose. The suspension contained trimers and a very small number of tetramers. The monomers obtained during the fractionation were used to calibrate the energy landscape as described below. An image of the trimers is shown in **Figure 1A**.

For the experiments, a dilute suspension of trimers was transferred into a quasi-two-dimensional cell consisting of a microscope slide and a cover slip [47], which were first carefully cleaned. The few pyramid-like tetramers present in the suspension served as spacers between the microscope slide and the cover slip. The confinement to quasi-two-dimensions reduces the degrees of freedom of each trimer to a center-of-mass translation and a rotation around one axis. Experiments were performed at a temperature of $\sim 20\,^{\circ}$C.

2.2. Random Light Field

The random light field is a speckle pattern (**Figure 1B**). It was generated as described previously [34]. The central optical element is a diffuser (RPC Photonics Inc., Engineered Diffuser^{TM} EDC-1-A-1r), which is illuminated with a planar wave with a Gaussian intensity distribution from a laser (Laser Quantum, Opus 532, wavelength $\lambda = 532$ nm). The diffuser creates a top-hat beam including a speckle pattern, which is directed to the sample plane of an inverted microscope. The average speckle size, which determines the correlation length of the light field, matches approximately the monomer size. The magnitude of the modulations is controlled via the laser power P_L. Four different laser intensities were applied: $P_L = 0$, 1.15, 1.60, and 2.10 W. The magnitude of the modulations also depends on the refractive index difference between the medium, in this case water with a refractive index of 1.330, and the PMMA particles with a refractive index of about 1.494 for the present wavelength.

2.3. Image Acquisition and Particle Tracking

The quasi-two-dimensional geometry allows us to use conventional optical microscopy. An inverted bright field microscope (Nikon, Eclipse Ti-U) with a 60× objective (Nikon, S Plan Fluor ELWD, NA 0.7) equipped with a CMOS camera (Allied Vision, Mako U-130B, 1,280 × 1,024 px^2) was used. The effective pixel pitch was 0.08 μm/px and the observation area was $\sim$ 100 × 82 μm^2. This area typically contained about 6 trimers.

Before each individual measurement, the diffuser was rotated in order to probe different realizations of the random potential. Then the sample was left to equilibrate for 30 min while it was exposed to the random light field. Subsequently, a series of 36,000 images was recorded at 10 fps resulting in an individual measurement time of 1 h. For each laser intensity, at least 15 individual measurements were performed, which resulted in a minimum of 90 trajectories. The measurements were controlled with a custom-written LabView programme. The positions and trajectories of individual spheres were extracted from the recorded images using a custom-written Matlab programme based on standard algorithms [48]. Based on these trajectories, the center-of-mass trajectories and the orientations of the trimers were determined.

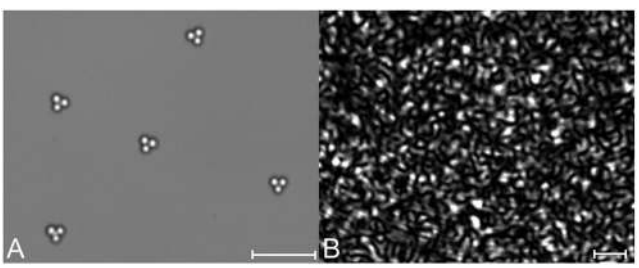

FIGURE 1 | (A) Optical microscopy image of trimers. **(B)** Random light field (speckle pattern) created by a diffuser illuminated with a laser beam. Particles exposed to such a light field experience a random potential energy landscape. Scale bars are 10 μm.

3. RESULTS AND DISCUSSION

We investigated trimers consisting of three joined spherical particles (**Figure 1A**). They were confined between two glass plates resulting in a quasi-two-dimensional system. Thus, their thermal motion contains two contributions: center-of-mass translation and rotation around the symmetry axis. The motion was modified by a random potential energy landscape whose values are drawn from a Gamma distribution with standard deviation ϵ and whose spatial correlation length is about the size of a spherical particle [34]. The magnitude of the modulations, quantified by ϵ, was varied with the maximum reaching a few times the thermal energy. This potential was imposed on the particles by applying a random light field and the magnitude of the modulations was controlled through the laser intensity P_L (**Figure 1B**). A convolution with the particle volume results in the potential energy landscape [34, 43, 49].

Examples of center-of-mass trajectories of trimers are shown in **Figure 2**. It illustrates the effect of the potential energy landscape on the translation of the trimers. Within the same time, trimers not exposed to a random potential explore a much larger region than trimers exposed to a random potential. The effect of the random potential on the translational motion will be quantified and compared to the effect on the rotational motion below. However, first the calibration of the random potential energy landscape will be explained.

3.1. Calibration of the Random Potential Energy Landscape—Translation of Spherical Particles

The magnitude of the modulations of the potential is estimated using the dynamics of spherical particles for which a theoretical prediction is available [50]. The dynamics of spherical particles, the building blocks of the trimers, are followed in the same random potential and characterized by the mean squared

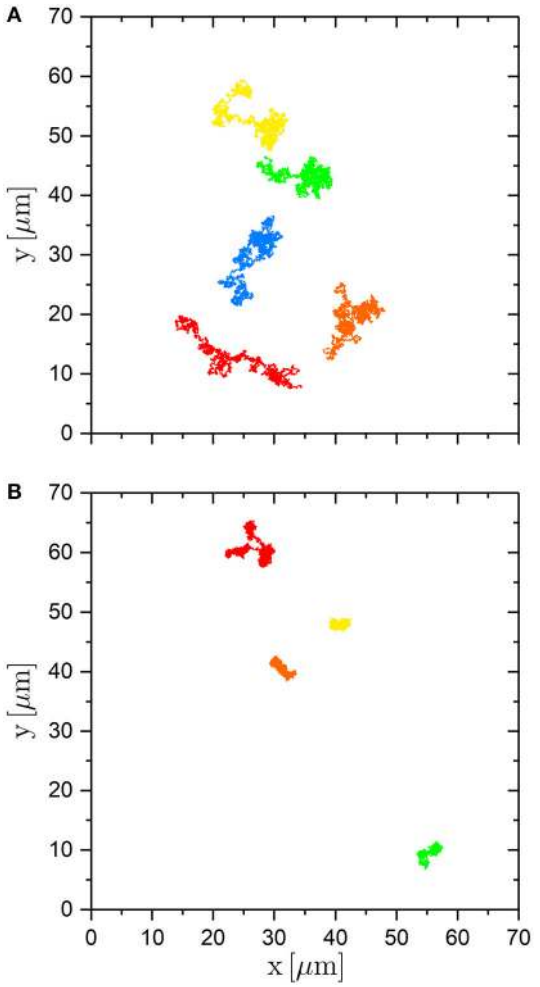

FIGURE 2 | Trajectories of the center-of-mass of trimers **(A)** in the absence of an external potential and **(B)** in the presence of an external potential created with the maximum laser intensity $P_L = 2.10$ W. The trajectories are followed for 60 min.

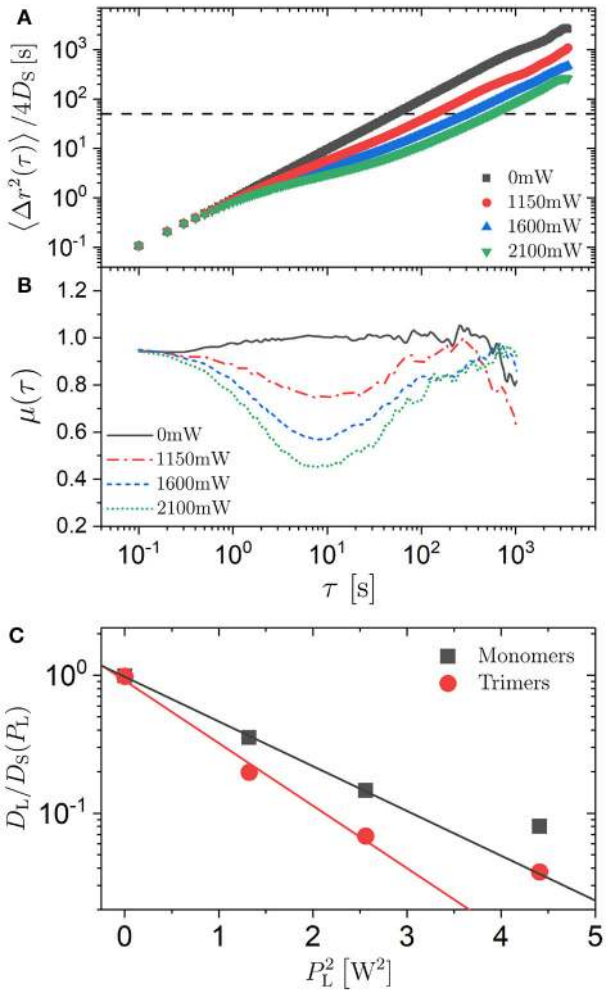

FIGURE 3 | (A) Mean squared displacement (MSD) $\langle \Delta r(\tau)^2 \rangle$ normalized by the short-time diffusion coefficient D_S and **(B)** exponent $\mu = \partial \log(\langle \Delta r(\tau)^2 \rangle)/\partial \log(\tau)$ as a function of delay time τ for spherical particles ("monomers") exposed to different laser intensities P_L (as indicated). The horizontal line in **(A)** indicates $\sigma^2/4D_S$. **(C)** Ratio of the long-time (D_L) to the short-time (D_S) diffusion coefficient as a function of the square of the laser intensity, P_L^2, of spherical particles (squares) and trimers (circles). The lines are linear fits to the data except at the highest P_L where D_L cannot be determined reliably.

displacement (MSD) [51]

$$\langle \Delta \mathbf{r}^2(\tau) \rangle = \langle [\mathbf{r}_i(t_0+\tau) - \mathbf{r}_i(t_0)]^2 \rangle_{i,t_0} , \quad (1)$$

where $\mathbf{r}_i(t)$ is the position of particle i at time t and the average is taken over all particles i and all start times t_0. This means that we consider the ensemble and time average. Without an external potential, the MSD increases linearly with delay time τ as expected (**Figure 3A**). In contrast, in the presence of an external potential, the MSD indicates different dynamic regimes: at short times diffusion, at intermediate times subdiffusion and at long times again diffusion but with a considerably reduced diffusion coefficient D_L. Whereas the diffusion at short times is not significantly affected by the external potential, the subdiffusion becomes more pronounced and the long-time diffusion increasingly slower with increasing laser intensity P_L. This can be quantified by calculating the exponent $\mu(\tau)$ in the relation $\langle \Delta \mathbf{r}^2(\tau) \rangle \sim \tau^{\mu(\tau)}$ from the slope of the MSD in double-logartihmic representation

$$\mu(\tau) = \frac{\partial \log \{ \langle \Delta \mathbf{r}^2(\tau) \rangle \}}{\partial \log \{\tau\}}. \quad (2)$$

The values of this parameter indicate initial diffusion ($\mu \approx 1$), intermediate subdiffusion with μ reaching values as small as about 0.5 and the re-establishment of diffusion at long times τ (**Figure 3B**). These observations agree with previous results [30, 39].

For a quantitative analysis, the confinement of the particles between two plates with only a small gap has to be considered.

Furthermore, radiation pressure pushes the particles in the direction of the laser beam and hence affects the distance between the particles and the two plates [27–29]. The resulting hydrodynamic interactions slow down diffusion regardless of whether there is an external potential [52, 53]. This results in a diffusion coefficient which is reduced compared to the bulk diffusion coefficient $D_0 = k_B T/(3\pi\eta\sigma)$, where η is the viscosity of the medium. Thus, the short-time diffusion coefficient D_S, which is affected by the hydrodynamic interactions with the plates but not by the external potential, was used to normalize the MSD and other dynamic parameters to account for the hydrodynamic interactions with the plates (**Figure 3A**). The short-time diffusion coefficient D_S was determined from the slope of the MSD at short times by

$$D_S = \frac{1}{4} \lim_{\tau \to 0} \left\{ \frac{\partial \langle \Delta \mathbf{r}^2(\tau) \rangle}{\partial \tau} \right\}. \quad (3)$$

It was found to increase by ∼12 % within the range of investigated laser intensities P_L (**Table 1**).

For the case of a random potential energy landscape with the energy values drawn from a Gaussian distribution with standard deviation ϵ, the long-time diffusion coefficient D_L is related to the short-time diffusion coefficient D_S by [50]

$$\frac{D_L}{D_S} = \exp\left[-\frac{1}{2} \left(\frac{\epsilon}{k_B T} \right)^2 \right]. \quad (4)$$

In our experiments, the energy values are Gamma distributed with a shape parameter $M \approx 1.7$ [34]. Assuming that the deviations from a Gaussian distribution are negligible, the experimentally determined ratio D_L/D_S can be used to relate the laser intensity P_L to the standard deviation of the energy distribution, ϵ. The long-time diffusion coefficient D_L was determined from the slope of the MSD at long times, analogous to the short-time diffusion coefficient D_S (Equation 3), if diffusion is re-established within the experimental time window. If this was not the case, D_L was determined based on the last data point at τ_{max}, $D_L = \langle \Delta \mathbf{r}^2(\tau_{max}) \rangle / 4\tau_{max}$ (or an average of the values from the last few data points), which is likely to overestimate D_L. Within the range of investigated laser intensities P_L, the ratio D_L/D_S decreases by slightly more than an order of magnitude (**Table 1**, **Figure 3C**) and using Equation (4) one obtains $\epsilon = 0.00$, 1.44, 1.92, and 2.25 $k_B T$, respectively. Thus, the magnitude of the modulations of the potential, ϵ, to which individual spherical particles and hence also each sphere forming a trimer is exposed, is linearly proportional to the laser intensity P_L at least for small P_L. This is indicated by the linear dependence of $\log(D_L/D_S)$ on P_L^2 (**Figure 3C**). The deviation from linearity at the largest $P_L = 2.10$ W could be due to a non-linearity between ϵ and P_L or the fact that diffusion is not re-established in the experimental window and hence D_L is overestimated and ϵ underestimated. The latter is more likely to be the reason. Due to this and the assumption concerning the distribution of energy values, in the following we will refer to the applied laser intensity P_L as a measure for the magnitude of the modulations of the random potential. Nevertheless, this analysis provides an estimate of the magnitude of the modulations which can reach a few times the thermal energy.

3.2. Translation of Trimers

3.2.1. Mean Squared Displacement

The MSD of the trimers was calculated following Equation (1) with $\mathbf{r}_i(t)$ now representing the trajectory of the center-of-mass of trimer i. As in the case of the spherical particles, the MSD was normalized by the short-time diffusion coefficient D_S to account for the hydrodynamic interactions with the glass plates. The hydrodynamic interactions depend on the separation of the trimers from the two plates which is affected by the radiation pressure and hence the laser intensity P_L. Within the range of investigated laser intensities P_L, the short-time diffusion coefficient D_S was found to increase by ∼25 % (**Table 1**). This increase is larger than for the spherical particles but still rather modest.

In the absence of a random potential, the MSD increases linearly with delay time τ over the whole investigated time window (**Figure 4A**) reflecting the expected free diffusion. In the presence of an external potential, however, different regimes are observed. At short delay times, a linear increase is observed which does not depend on laser intensity P_L because the time

TABLE 1 | Diffusion coefficients for particles exposed to different laser intensities P_L: short-time diffusion coefficient D_S for spherical particles, ratio of the long-time to the short-time diffusion coefficient (D_L/D_S) for spherical particles, short-time translational diffusion coefficient D_S for the center-of-mass motion of trimers, ratio of the long-time to the short-time translational diffusion coefficient (D_L/D_S) for the center-of-mass motion of trimers, short-time rotational diffusion coefficient D_S^{rot} for trimers, ratio of the long-time to the short-time rotational diffusion coefficient (D_L^{rot}/D_S^{rot}) for trimers, mean residence time $\langle \Delta t \rangle$ (where the ranges indicate the uncertainties of the fits), mean residence time estimated from the ratio of the total measurement time T_m to the total number of jumps N_m, ratio of the long-time to the short-time rotational diffusion coefficient (D_L^{rot}/D_S^{rot}) for trimers calculated based on the mean residence time $\langle \Delta t \rangle$.

	Monomer		Trimer						
	Translation		Translation		Rotation		Rotation (calculated)		
P_L [W]	D_S [$\mu m^2/s$]	D_L/D_S	D_S [$\mu m^2/s$]	D_L/D_S	D_S^{rot} [rad^2/s]	D_L^{rot}/D_S^{rot}	$\langle \Delta t \rangle$ [s]	T_m/N_m [s]	D_L^{rot}/D_S^{rot}
0	0.022	0.99	0.0089	0.98	0.013	1.03	159 ± 3	178	1.07
1.15	0.024	0.35	0.0092	0.20	0.013	0.81	185 ± 2	215	0.90
1.60	0.023	0.15	0.0096	0.07	0.014	0.77	214 ± 6	254	0.76
2.10	0.024	0.08	0.0112	0.04	0.015	0.60	230 ± 5	275	0.62

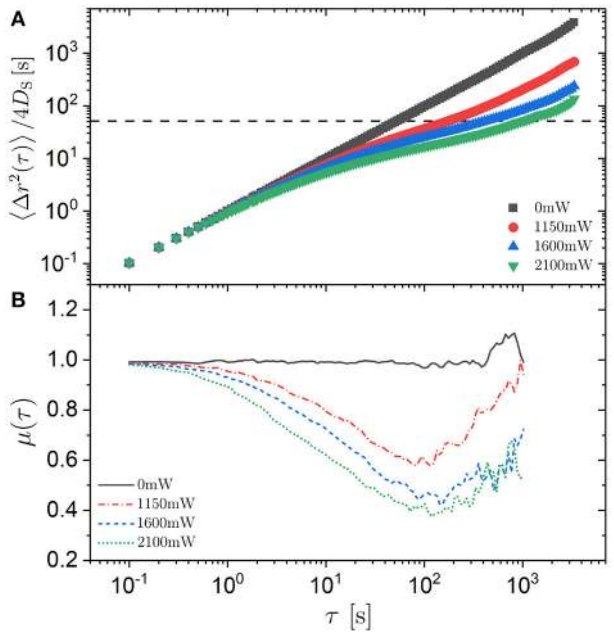

FIGURE 4 | (A) Mean squared displacement (MSD) $\langle \Delta r(\tau)^2 \rangle$ normalized by the short-time diffusion coefficient D_S and **(B)** exponent $\mu = \partial \log(\langle \Delta r(\tau)^2 \rangle)/\partial \log(\tau)$ as a function of delay time τ for the center-of-mass of trimers exposed to different laser intensities P_L (as indicated). The horizontal line in **(A)** indicates $\sigma^2/4D_S$.

and distances traveled during this time are too short for the trimer to experience significant changes of the external potential. Subsequently, subdiffusion is indicated by a slope μ smaller than 1 with the slope decreasing upon increasing the laser intensity P_L (**Figure 4B**). This is due to the confinement of the trimer to a potential minimum or the confinement of the constituent three spheres to neighboring potential minima. The trimers wiggle within the minima but they do not leave the minima within this time scale. The potential minima correspond to the randomly distributed bright speckles in the light pattern that have an average size of about 2 μm (**Figure 1B**) similar to the sphere diameter $\sigma \approx 2.1$ μm (**Figure 4A**, dashed horizontal line). The relatively small values of $\langle \Delta \mathbf{r}^2(\tau) \rangle$ in the intermediate regime indicate that the trimers only explore the central part of the minima. A slope $\mu \approx 1$ is again reached and hence diffusion is re-established at very long times. This time scale is long enough for the trimers to leave the minima and move from minimum to minimum in a random fashion. The ratio of the long-time to the short-time diffusion coefficient (D_L/D_S) shows a major decrease by about one and a half order of magnitude within the range of investigated laser intensities P_L (**Table 1**, **Figure 3C**). Thus it is significantly more pronounced than for spherical particles. The dependence of $\log(D_L/D_S)$ on P_L^2 is linear except for the largest laser intensity $P_L = 2.10$ W, which again is attributed to the difficulty in reliably determining the long-time diffusion coefficient D_L in this case because the long-time diffusive regime is not reached within the experimental time window (**Figure 4B**). The linear dependence is consistent with Equation (4). Moreover, the MSDs of the trimers and of the spherical particles, the "monomers," show similar behavior over the whole experimental time window (**Figures 3A**, **4A**). The dependences of the long-time diffusion coefficient D_L on the laser intensity P_L also show comparable trends but the D_L of the trimers is significantly smaller (**Figure 3C**), which is due to the stronger effect of the light field on the three spheres forming the trimers than on an individual sphere. Nevertheless, there are quantitative differences. In the case of trimers, the subdiffusive regime starts at larger delay times and extends to longer times (**Figures 3B**, **4B**).

3.2.2. Self Part of the van Hove Function

While the mean squared displacement characterizes the width of the distribution of displacements, more detailed information on the dynamics can be obtained by examining the distribution of displacements itself. The probability to find a particle at position $\mathbf{r} + \Delta\mathbf{r}$ at time $t_0 + \tau$ given that there was a particle at position $\mathbf{r}$ at time t_0 is given by the van Hove function

$$G(\Delta\mathbf{r}, \tau) = \frac{1}{N} \left\langle \sum_{i=1}^{N} \sum_{j=1}^{N} \delta\{\Delta\mathbf{r} - [\mathbf{r}_i(t_0+\tau) - \mathbf{r}_j(t_0)]\} \right\rangle_{t_0}, \quad (5)$$

where the average is taken over the start time t_0. The van Hove function can be separated in a self ($i = j$) and distinct ($i \neq j$) part. Here we focus on the motion of individual particles and hence are interested in the self part of the van Hove function

$$G_s(\Delta\mathbf{r}, \tau) = \frac{1}{N} \left\langle \sum_{i=1}^{N} \delta\{\Delta\mathbf{r} - [\mathbf{r}_i(t_0+\tau) - \mathbf{r}_i(t_0)]\} \right\rangle_{t_0}. \quad (6)$$

For an isotropic particle undergoing free diffusion, the self part of the van Hove functions is a Gaussian distribution with mean zero and the square of the standard deviation represented by the MSD.

Based on the trajectories, the self part of the van Hove function $G_s(\Delta\mathbf{r}, \tau)$ can be calculated for the different laser intensities P_L. We consider the individual components of the displacement vector $\Delta\mathbf{r}$, namely Δx and Δy, as well as its magnitude, Δr (**Figure 5**). In the absence of the random potential, in other words in the case of free diffusion, the self part of the van Hove function $G_s(\Delta x, \tau)$ shows the expected Gaussian shape with the width increasing with delay time τ. If the random potential is present, at intermediate delay times the distribution is narrower. This corresponds to the sublinear increase of the MSD with delay time τ and is due to the fact that the trimers remain in the central part of the potential minima for some time. At longer delay times, the self part of the van Hove function develops shoulders on both sides of the central maximum and minor maxima at $\Delta x \approx -4\,\mu$m and $\Delta x \approx 4\,\mu$m. These shoulders become more pronounced for longer delay times τ and larger laser intensities P_L. They reflect the random motion between minima that are randomly distributed and separated by a few μm (**Figure 1B**). Furthermore, the shape of $G_s(\Delta x, \tau)$ increasingly deviates from

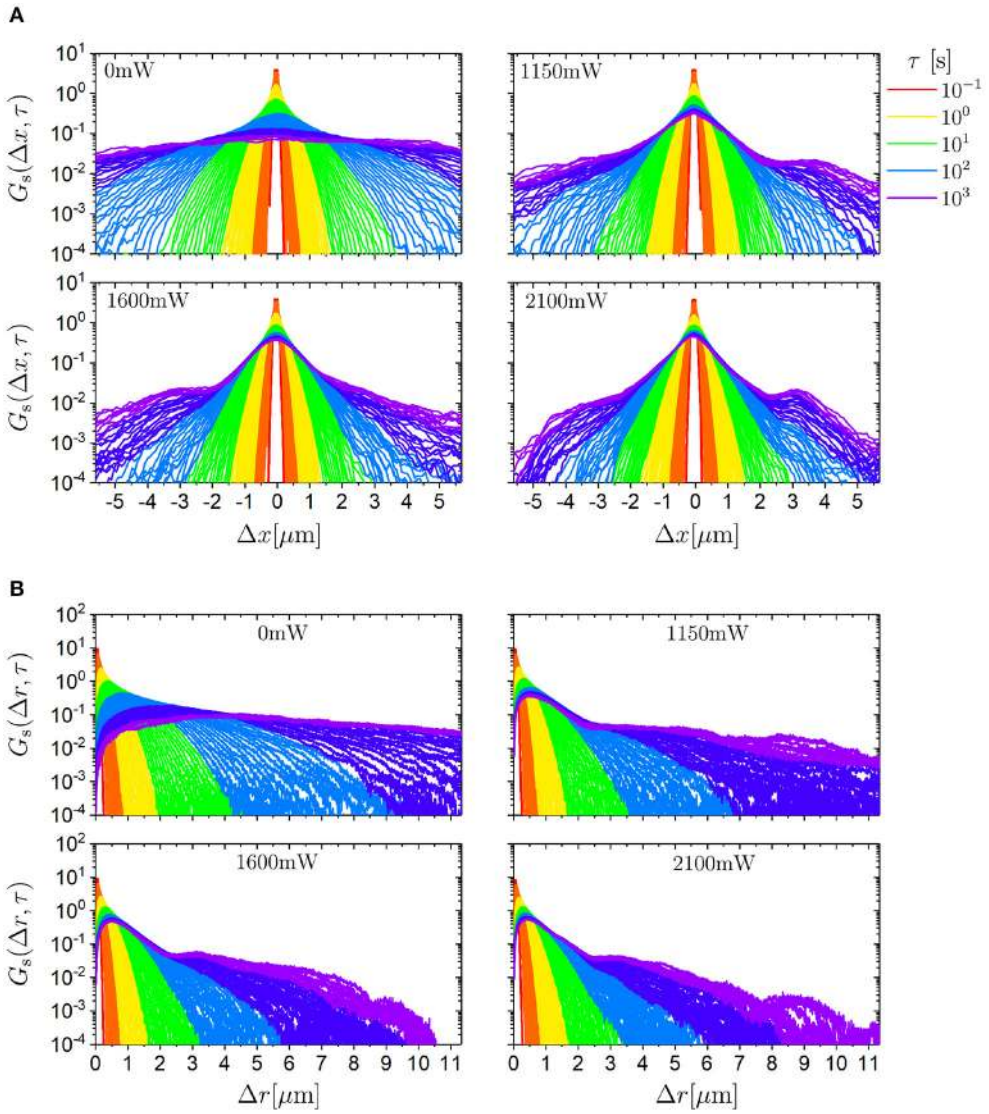

FIGURE 5 | Self part of the van Hove function G_s for **(A)** displacements in x direction (Δx) and **(B)** modulus of the displacement vector (Δr) for different delay times τ (indicated by the color) for trimers exposed to different laser intensities P_L (as indicated).

a Gaussian shape and, at long times, can better be described by a Laplacian shape.

The distribution of the magnitude of the displacement, $G_s(\Delta r, \tau)$ (**Figure 5B**), resembles the expected Rayleigh distribution in the absence of the random potential. In the presence of the random potential, the evolution with delay time τ and laser intensity P_L corresponds to the dependence observed in $G_s(\Delta x, \tau)$. These are a limited broadening of the main peak and the development of shoulders and minor maxima at intermediate and long times.

3.2.3. Non-gaussian Parameter

Since the self part of the van Hove function $G_s(\Delta x, \tau)$ is not Gaussian in the presence of the random potential (**Figure 5A**), it cannot be fully characterized by only the MSD (**Figure 4A**) but further moments are required. Thus, the fourth moment is considered, which usually is normalized to yield the non-Gaussian parameter $\alpha_2(\tau)$ [54]. We focus on the distributions of one-dimensional displacements, $G_s(\Delta x, \tau)$, and hence use the corresponding non-Gaussian parameter defined for one dimension [55]

$$\alpha_2(\tau) = \frac{\langle \Delta x^4(\tau) \rangle}{3 \langle \Delta x^2(\tau) \rangle^2} - 1 \tag{7}$$

and similarly for the y direction. Other definitions of the non-Gaussian parameter have been proposed, for example [56], which only differ by a constant factor. Since $\alpha_2(\tau)$ contains a higher order moment than the MSD, it is more prone to noise and

hence has to be based on more data pairs for comparable statistics implying a more restricted range of delay times τ.

The non-Gaussian parameter $\alpha_2(\tau)$ was determined for Δx and Δy, which, not surprisingly, show similar behavior (**Figure 6**). As expected, in the absence of an external potential the non-Gaussian parameter $\alpha_2(\tau) \approx 0$. In the presence of an external potential, $\alpha_2(\tau) \approx 0$ at short times and hence small traveled distances, during which no significant changes of the external potential are experienced. However, at intermediate times $\alpha_2(\tau)$ increases, reaches a maximum and decreases again. The maximum reaches values as large as $\alpha_2 \approx 2.5$. This large value reflects the pronounced tails and minor maxima in the self part of the van Hove function $G_s(\Delta x, \tau)$ (**Figure 5**). The maximum is located at the transition from the intermediate subdiffusion to the long-time diffusion (**Figure 4**) because, at this time, many trimers still reside in their initial minima while a similarly large number of trimers have already moved to other minima and thus the ensemble of trimers exhibits very heterogeneous dynamics. Once most of the trimers have moved to other minima and diffusion is re-established, the non-Gaussian parameter $\alpha_2(\tau)$ returns to zero.

3.3. Rotation of Trimers

The rotation of a trimer can be deduced from the position of its three constituent spheres. One of the three spheres is chosen arbitrarily. The line connecting the center-of-mass of the trimer with the center of this sphere is considered to be the direction of the trimer (**Figure 7A**, arrow in inset). The angle between this line and an arbitrary but fixed direction (here the x direction) is taken to quantify the orientation of the trimer. This angle $\theta_i(t)$ is followed as a function of time t for each trimer i. Based on $\theta_i(t)$ the rotational dynamics can be investigated.

3.3.1. Mean Squared Angular Displacement

In analogy to Equation (1), the mean squared angular displacement (MSAD) is defined as

$$\langle \Delta\theta^2(\tau) \rangle = \langle [\theta_i(t_0+\tau) - \theta_i(t_0)]^2 \rangle_{i,t_0} \, . \tag{8}$$

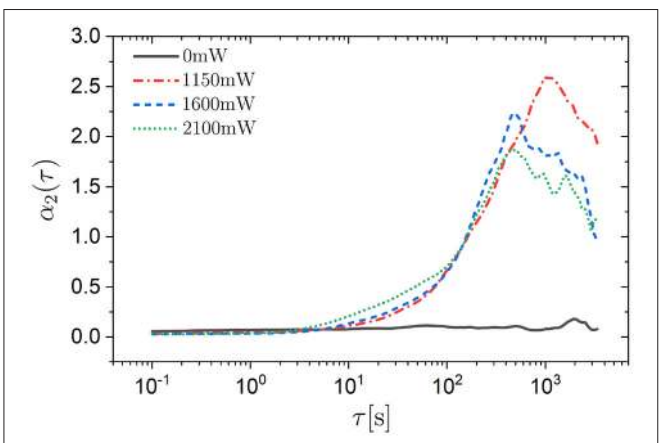

FIGURE 6 | Non-Gaussian parameter $\alpha_2(\tau)$ for displacements in the x direction as a function of the delay time τ for trimers exposed to different laser intensities P_L (as indicated).

The MSAD was determined based on the experimentally observed $\theta_i(t)$. Similar to the analysis of the translational motion, the MSAD was normalized by the short-time rotational diffusion coefficient D_S^{rot} to account for the effects of hydrodynamic interactions. Similar to the short-time diffusion coefficient D_S, the short-time rotational diffusion coefficient D_S^{rot} is affected by the hydrodynamic interactions but hardly affected by the external potential. It was determined from the slope of the MSAD at short times, analogous to the determination of D_S (Equation 3). The frame rate was chosen to be fast enough (10 fps) for a reliable determination of the initial slope. The short-time rotational diffusion coefficient D_S^{rot} increases within the investigated range of laser intensities P_L by $\sim 20\,\%$ (**Table 1**) which is similar to

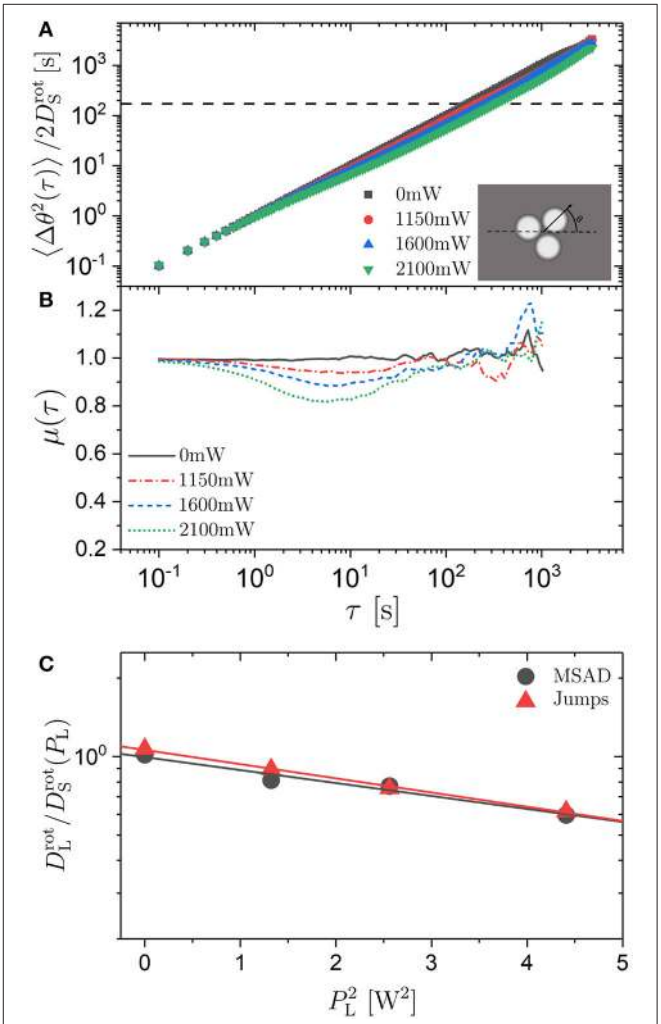

FIGURE 7 | (A) Mean squared angular displacement (MSAD) $\langle \Delta\theta(\tau)^2 \rangle$ normalized by the short-time rotational diffusion coefficient D_S^{rot} and **(B)** exponent $\mu = \partial \log(\langle \Delta\theta(\tau)^2 \rangle) / \partial \log(\tau)$ as a function of delay time τ for trimers exposed to different laser intensities P_L (as indicated). The horizontal line in (A) indicates $(120^\circ)^2 / 2D_S^{rot}$. **(C)** Ratio of the long-time (D_L^{rot}) to the short-time (D_S^{rot}) rotational diffusion coefficient as a function of the square of the laser intensity, P_L^2, for trimers as determined from the MSAD (circles) and calculated based on the jump statistics (triangles). The lines are linear fits.

the increase of the short-time diffusion coefficient D_S of the center-of-mass diffusion of trimers.

The normalized MSAD was calculated for all laser intensities P_L (**Figure 7A**). The effect of the external potential on the MSAD is modest. At intermediate times the slope is only slightly smaller than unity ($\mu > 0.8$ for all P_L, **Figure 7B**) and the reduction of the long-time diffusion coefficient D_L^{rot} is very limited (**Figure 7C**). The ratio of the long-time to the short-time rotational diffusion coefficient (D_L^{rot}/D_S^{rot}) decreases by less than a factor of 2 within the range of investigated laser intensities P_L. The modest decrease of the long-time rotational diffusion coefficient D_L^{rot} is in strong contrast to the pronounced effect of the external potential on the long-time translational diffusion coefficient D_L (**Figure 3C**). However, $\log(D_L^{rot}/D_S^{rot})$ decreases linearly with the square of the laser intensity, P_L^2 similar to D_L (**Figure 7C**, Equation 4). Moreover, the intermediate subdiffusion of the rotational motion is not only much less pronounced than the one for the translational motion, it also occurs significantly earlier than the one for the translational motion: at times about an order of magnitude smaller (**Figure 4B**). This time window is comparable to the one during which the intermediate subdiffusion of individual spheres is observed (**Figure 3B**).

3.3.2. Self Part of the van Hove Function and Non-gaussian Parameter

Despite the innocuous-looking MSAD, we determined the self part of the van Hove function for angular displacements, $G_s(\Delta\theta, \tau)$ (defined analogous to Equation 6). Overall, $G_s(\Delta\theta, \tau)$ has a Gaussian shape with the width increasing with delay time τ (**Figures 8A–D**). Nevertheless, with increasing delay time τ and especially with increasing laser intensity P_L oscillations emerge which are separated by about 120°. The effect of increasing P_L, which increases the magnitude of the modulations of the potential, while keeping the delay time constant (data are averaged over the interval 35 min $< \tau <$ 60 min) is illustrated

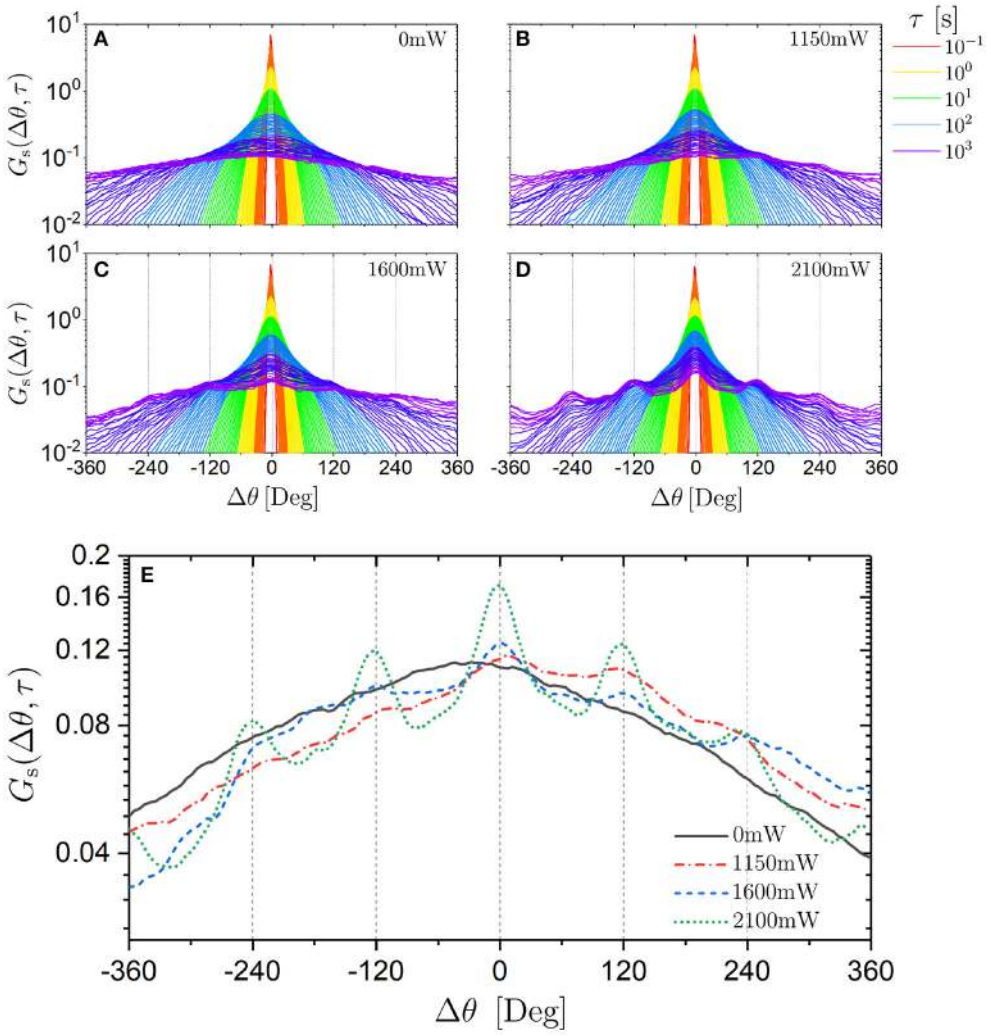

FIGURE 8 | Self part of the van Hove function $G_s(\Delta\theta, \tau)$ for angular displacements $\Delta\theta$ for trimers exposed to different laser intensities P_L (as indicated) **(A–D)** for different delay times τ (indicated by the color) and **(E)** for a long delay time (averaged over delay times 35 min $< \tau <$ 60 min) for different P_L (as indicated).

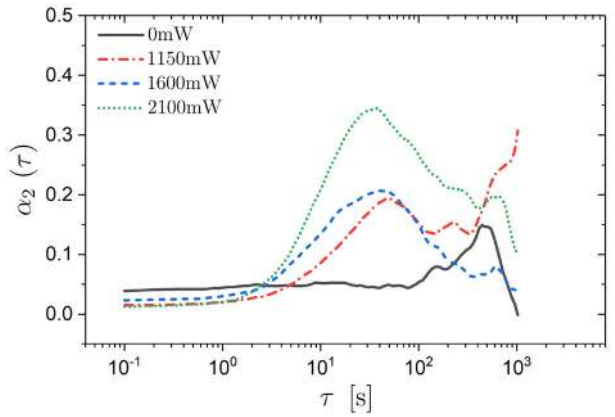

FIGURE 9 | Non-Gaussian parameter $\alpha_2(\tau)$ for rotational displacements $\Delta\theta$ as a function of delay time τ for trimers exposed to different laser intensities P_L (as indicated).

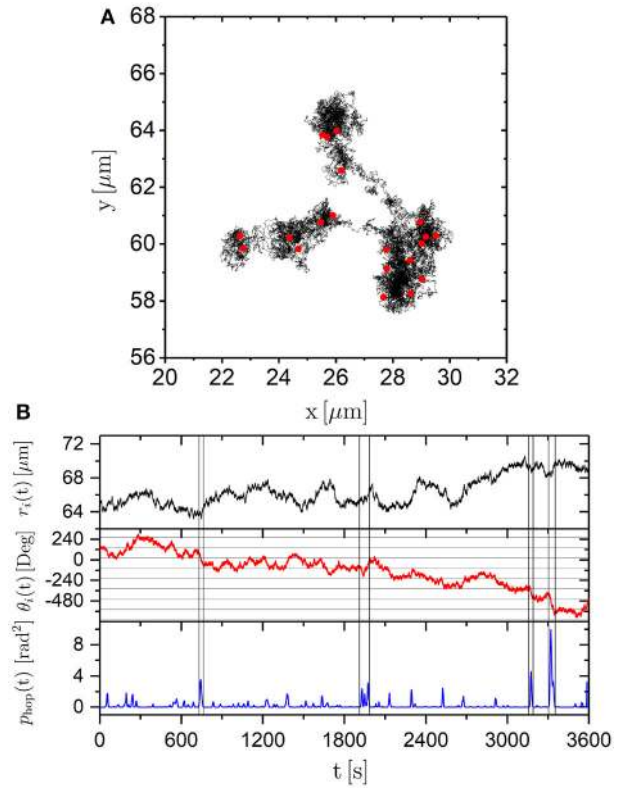

FIGURE 10 | (A) Trajectory of a trimer exposed to a laser intensity P_L = 2.10 W lasting 1 h. Red points indicate angular jumps defined by $p_{hop} > 0.75$ rad^2. **(B)** Corresponding time-dependence of the center-of mass $r_i(t)$ (top), orientation $\theta_i(t)$ (middle) and angular hop identifier $p_{hop}(t)$ (bottom). The vertical lines indicate regions of large values of $p_{hop}(t)$.

in **Figure 8E**. The data suggest that the trimers perform discrete rotational jumps of about 120° which become increasingly important as the magnitude of the modulations of the potential is increased. (Note that, although there are characteristic rotational jumps with $\Delta\theta \approx 120°$, the orientations of the trimers, $\theta_i(t)$, remain random). Whereas the oscillations become significantly more pronounced, in particular at the highest laser intensity, the overall Gaussian shape is hardly affected by the external potential. This is consistent with the non-Gaussian parameter $\alpha_2(\tau)$ (**Figure 9**). It only shows a moderate maximum ($\alpha_2 \approx 0.3$) which is approximately an order of magnitude smaller than the maximum observed in the $\alpha_2(\tau)$ of the translational motion (**Figure 6**). Furthermore, the time window during which the non-Gaussian parameter is significantly different from zero occurs much earlier for rotational motion than the corresponding time window of the translational motion (**Figure 6**): again by approximately an order of magnitude.

3.3.3. Angular Jumps

A typical trajectory $\mathbf{r}_i(t)$ of a particle exposed to a high laser intensity $P_L = 2.10$ W lasting 1 h is shown in **Figure 10A**. The trajectory indicates that the trimer remains in a limited area for some time before moving on. The size of these areas is about 2 μm, which is similar to the speckle size (**Figure 1B**). This suggests that the trajectories reflect the wiggling in minima as well as the motion between minima as is also indicated by the MSD (**Figure 4A**). The corresponding time evolutions of the center-of-mass, $r_i(t)$, and of the orientation, $\theta_i(t)$, are shown in **Figure 10B**. They show many small displacements and a few larger displacements of the center-of-mass, $r_i(t)$, as well as of the orientation, $\theta_i(t)$. To analyse the discrete angular jumps suggested by the self part of the van Hove function, $G_s(\Delta\theta, \tau)$ (**Figure 8**), a previously proposed algorithm based on the so-called hop identifier function $p_{hop}(t)$ [57, 58] was adapted. It detects major changes of the orientation occurring during a time interval T centered around the time t. The evolution of the orientation during the two neighboring time periods $[t-T/2, t]$, and $[t, t+T/2]$ (labeled A and B, respectively), is considered. The average orientations during the two periods $\langle\theta_i(t)\rangle_{t\in A}$ and $\langle\theta_i(t)\rangle_{t\in B}$ are determined. Then the hop identifier function $p_{hop}(t)$ is calculated which compares the values in one of the periods with the average during the other period. It is defined as

$$p_{hop}(t) = \sqrt{\left\langle[\theta_i(t') - \langle\theta_i(t'')\rangle_{t''\in B}]^2\right\rangle_{t'\in A} \left\langle[\theta_i(t'') - \langle\theta_i(t')\rangle_{t'\in A}]^2\right\rangle_{t''\in B}}. \quad (9)$$

Here we consider a time interval $T = 15$ s, which corresponds to 150 points in the trajectory and sweeps over the experimentally observed angular traces $\theta_i(t)$. With the help of p_{hop} major changes in $\theta_i(t)$ were identified with the value of p_{hop} characterizing the magnitude and temporal extent of the change. A large value of p_{hop} indicates large changes in the orientation during a short time (**Figure 10B**). The magnitude of the angular change $\Delta\Theta_i(t_j)$ of trimer i at time t_j is defined as

$$\Delta\Theta_i(t_j) = |\langle\theta_i(t')\rangle_{t'\in\mathbb{A}} - \langle\theta_i(t')\rangle_{t'\in\mathbb{B}}|, \quad (10)$$

where the averages are taken over the time intervals before and after the jump at time t_j, i.e., $\mathbb{A} = [t_{j-1} + T/2, t_j - T/2]$ and

$\mathbb{B} = [t_j + T/2, t_{j+1} - T/2]$, respectively. (Note that, in contrast, $\Delta\theta_i(\tau, t) = \theta_i(t+\tau) - \theta_i(t)$ represents the difference between two instantaneous angles).

We consider changes in the angular trace corresponding to $p_{\text{hop}}(t_j) > 0.75$ rad^2 as significant changes ("jumps") occurring at time t_j. Smaller threshold values were found to be too close to the noise level and hence to yield unreliable results. In **Figure 10A** red dots indicate where angular jumps occurred along the trajectory. Several angular jumps occur while the trimer remains in an individual minima. Therefore, the angular jumps are not related to escapes from minima. This can also be seen from a comparison of $r_i(t)$ and $p_{\text{hop}}(t)$. At times t_j where $p_{\text{hop}}(t_j)$ shows a peak and hence indicates a jump in $\theta_i(t)$, the translational motion $r_i(t)$ does not show significant changes or jumps. Thus, based on $p_{\text{hop}}(t)$, angular jumps can be identified but they seem uncorrelated with the translational motion. Angular jumps have previously been observed for the motion of dimers exposed to a periodic potential energy landscape created by a fringe pattern [43]. In this study, rotations within the one-dimensional potential minima have been experimentally observed and theoretically predicted to occur through discrete rotational jumps. These rotational jumps were found to be coupled to the translational motion.

Having identified the angular jumps, the occurrences of clockwise and counter-clockwise jumps were compared. They are equally likely and independent of the previous jump direction. The ratios of the probabilities for clockwise and counter-clockwise jumps were found to be between 0.989 and 1.011 for the different laser intensities P_L and do not show a dependence on the laser intensities P_L (taking into account a total of 6,615 jumps during a total measurement time of $\sim$ 235 h). Thus, memory effects are absent for all investigated laser intensities P_L.

The probability distribution of the magnitude of angular jumps, $p(\Delta\Theta)$, was investigated. Again, $p_{\text{hop}}(t_j) > 0.75$ rad^2 is taken to indicate jumps. This criterion suppresses small $\Delta\Theta$ and hence the resulting distribution will not represent the true distribution reliably at small $\Delta\Theta$ ($\Delta\Theta < \sqrt{0.75}$ rad $\approx 50^\circ$) and, depending on the temporal extent of the jumps, at larger values of $\Delta\Theta$. Despite these shortcomings, we will continue with this analysis. In addition to the anticipated suppression of small values of $\Delta\Theta$, $p(\Delta\Theta)$ decreases for increasingly large jumps (**Figure 11A**). In the absence of an external potential, the decrease of $p(\Delta\Theta)$ follows a Gaussian distribution as expected. With increasing laser intensity P_L, $p(\Delta\Theta)$ keeps its overall shape but shows a high probability for jumps with $\Delta\Theta \approx 120^\circ$. This is in agreement with the increasingly more pronounced oscillations in $G_s(\Delta\theta, \tau)$ (**Figure 8**) and supports the idea of discrete angular jumps with $\Delta\Theta \approx 120^\circ$.

Based on $p_{\text{hop}}(t)$, the residence time between two jumps, $\Delta t = t_j - t_{j-1}$, can be extracted as the time elapsed between two consecutive occurrences of $p_{\text{hop}}(t_j) > 0.75$ rad^2 and the distribution of residence times, $p(\Delta t)$, determined. The times are found to be exponentially distributed for all laser intensities P_L (**Figure 11B**) as expected for a Poisson process. An exponential fit provides the mean residence time $\langle\Delta t\rangle$. It ranges from $\sim$ 160 to 230 s with increasing laser intensity P_L (**Table 1**). These values can be compared to the mean residence times estimated from the ratio of the total measurement time T_m and the total number of jumps during this time, N_m, where $T_m \approx 100$ h and $N_m \approx 1{,}700$ for each laser intensity (**Table 1**). The values are in reasonable agreement given the different weightings involved in the two approaches.

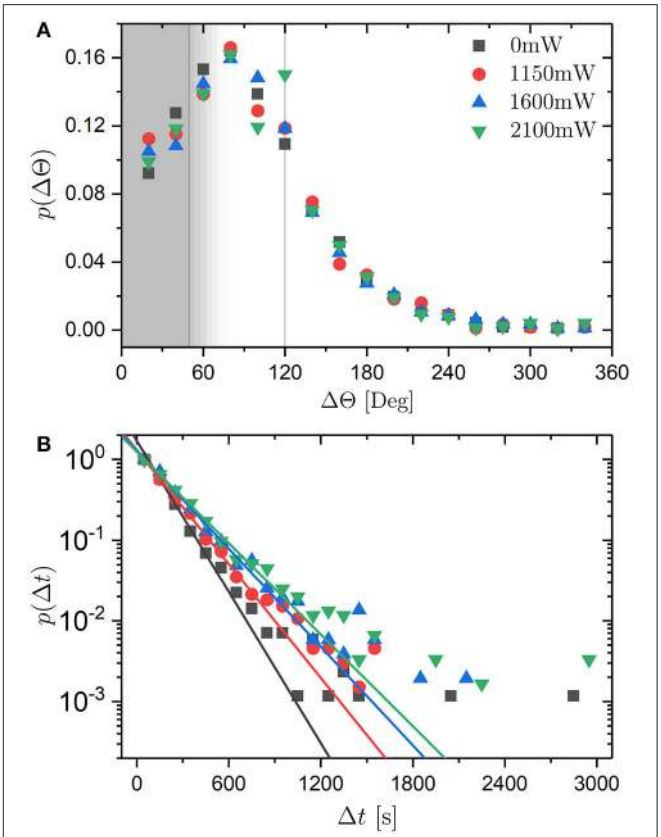

FIGURE 11 | (A) Probability distribution $p(\Delta\Theta)$ of angular jumps $\Delta\Theta$ for different laser intensities P_L (as indicated). Angular jumps are identified by $p_{\text{hop}}(t) > 0.75$ rad^2 which implies that small jumps with $\Delta\Theta < \sqrt{0.75}$ rad $\approx 50^\circ$ are suppressed (vertical line in gray area) and, depending on the temporal extent of the jumps, jumps with larger values of $\Delta\Theta$ (gray area). **(B)** Probability distribution $p(\Delta t)$ of residence times Δt for different laser intensities P_L (as indicated). Straight lines represent exponential fits to $p(\Delta t)$ at small Δt.

Based on the second moment of $p(\Delta\Theta)$ and the mean of $p(\Delta t)$, the long-time rotational diffusion coefficient D_L^{rot} can be calculated assuming that the jumps dominate the long-time rotational diffusion:

$$D_L^{\text{rot}} = \frac{\langle\Delta\Theta^2\rangle}{2\langle\Delta t\rangle}\,, \tag{11}$$

where we take $\langle\Delta\Theta^2\rangle = (120^\circ)^2 = (2.09 \text{ rad})^2$. With the values of $\langle\Delta t\rangle$ given above, D_L^{rot} can be calculated for the different P_L (**Table 1**). The calculated values are in very good agreement with the experimentally determined values (**Figure 7C**).

3.3.4. Link Between Rotation and Translation

Above we considered the self part of the van Hove function for angular displacements $G_s(\Delta\theta, \tau)$ as a function of delay

time τ (**Figure 8**). To investigate the correlation between rotation (angular displacements $\Delta\theta$) and translation (spatial displacements Δr), the self part of the van Hove function for angular displacements $G_s(\Delta\theta, \Delta r)$ as a function of displacements Δr is considered [**Figures 12A–D** which for clarity shows $G_s(|\Delta\theta|, \Delta r)$ instead of the symmetrical $G_s(\Delta\theta, \Delta r)$]. Without an external potential, $G_s(\Delta\theta, \Delta r)$ broadens with increasing Δr. As the translational displacement Δr increases, larger angular displacements $\Delta\theta$ also become more likely. In the presence of an external potential, $G_s(\Delta\theta, \Delta r)$ also broadens and in addition develops characteristic maxima. This indicates that the particles have preferences for specific angular displacements $\Delta\theta$. With increasing laser intensity P_L, the maxima become more pronounced but the general behavior remains similar. For small $\Delta r \lesssim 0.8\,\mu$m, large values of $G_s(\Delta\theta, \Delta r)$ are observed at multiples of 120°. This is consistent with the jumps of 120° discussed above and demonstrated, for example, by maxima in $G_s(\Delta\theta, \tau)$ separated by $\sim$ 120° (**Figure 8**) or by the high probability for jumps with $\Delta\Theta \approx 120°$ in $p(\Delta\Theta)$ (**Figure 11A**). Since the displacements of the center-of-mass are quite small, these observations reflect rotations of the trimers with the spheres swapping their locations but the center-of-mass of the trimer essentially remaining in the same position (**Figure 13A**). This explains why no significant translational displacements are observed when angular jumps are identified (**Figure 10B**) and hence why the rotation and translation appear uncorrelated based on $p_{hop}(t)$. Upon increasing the translational displacements to $0.8\,\mu\text{m} \leq \Delta r \leq 1.4\,\mu$m, the maxima at multiples of 120° vanish and instead maxima at 60° and much smaller maxima at 180° and 300° emerge. This is consistent with two minima remaining occupied while one neighboring minimum is newly occupied (**Figure 13B**) because, in an idealized situation, this involves a rotation by 60° and possible further rotations by multiples of 120° in addition to a translational motion by $\sigma/\sqrt{3} \approx 1.2\,\mu$m. Therefore, in this case, a rotation of 60° is coupled to a translation of about $\sigma/\sqrt{3}$. This coupling of translation and rotation could not be detected with the hop identifier because it cannot reliably identify a jump of 60° with the criterion $p_{hop}(t_j) > 0.75$ rad^2. Larger translational motions ($\Delta r > 1.4\,\mu$m) imply that at most one minimum remains occupied whereas two neighboring minima are newly occupied. If one minimum remains occupied, this involves in the idealized case shown in **Figure 13C** a rotation between 120° and 180° and possibly further rotations by multiples of 120° as well as a displacement $\sigma \leq \Delta r \leq 2\sigma/\sqrt{3}$. Moreover, a motion to new minima can involve any rotation and any displacement with $\Delta r \gtrsim \sigma$. This is reflected in the broad distribution of angular displacements and the lack of a preference for a specific angular displacement for large translational displacements $\Delta r \gtrsim 1.6\,\mu$m. This is qualitatively different from the van Hove function for angular displacements as a function of delay time τ, $G_s(\Delta\theta, \tau)$, which also shows maxima at specific angular displacements at long delay times τ (**Figure 8**). This preference of $G_s(\Delta\theta, \tau)$ for specific angular displacements can be maintained during long time periods because a long time period does not necessarily imply significant translational motion during which any angular displacement can occur but does allow for negligible translational motion while a swap of the positions of the spheres results in a rotation by a multiple of 120° (**Figure 13A**). Thus, the coupling between translation and rotation depends on the distance the

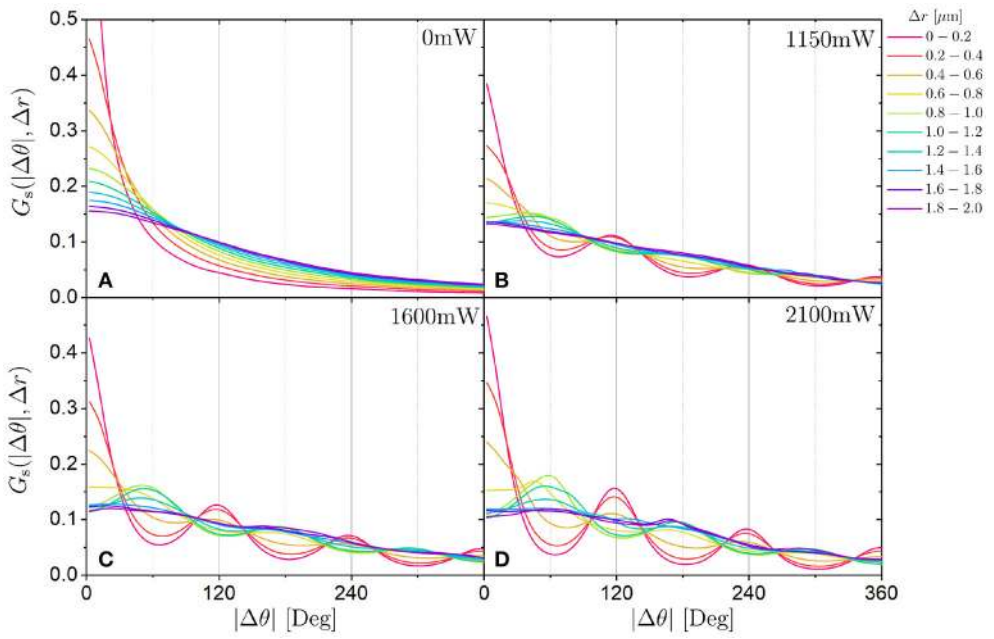

FIGURE 12 | Self part of the van Hove function $G_s(|\Delta\theta|, \Delta r)$ for angular displacements $|\Delta\theta|$ for different translational displacements Δr (indicated by the color) for trimers exposed to different laser intensities P_L (as indicated, **A–D**). Note that $G_s(\Delta\theta, \Delta r)$ is symmetrical and hence $G_s(|\Delta\theta|, \Delta r)$ is shown for clarity.

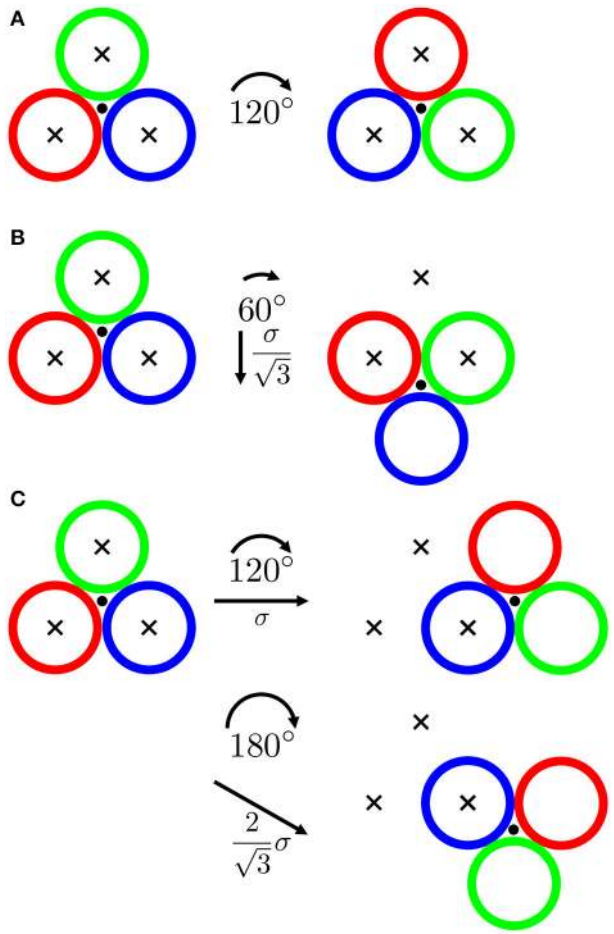

FIGURE 13 | Schematic representation of a trimer (differently colored open circles) undergoing rearrangements involving **(A)** three, **(B)** two and **(C)** one initial minima remaining occupied as well as the corresponding angular ($\Delta\theta$, arcs) and translational (Δr, arrows), displacements. The center-of-mass is indicated by a filled circle and the initially occupied minima are indicated by crosses. The particle size and the speckle size are assumed to be equal. Idealized situations with all three spheres initially perfectly placed in minima are represented here. This does not fully reflect the random nature of the potential but may reasonably approximate the actually occupied locations with low potential energies for the whole trimer.

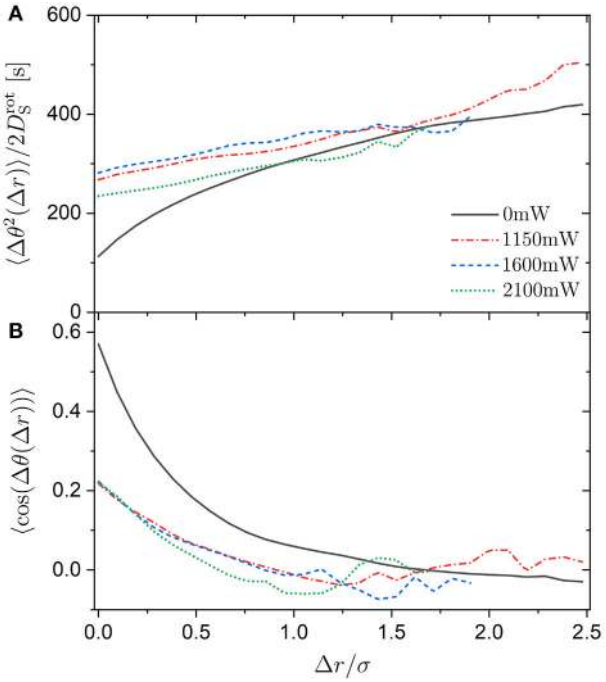

FIGURE 14 | (A) Mean squared angular displacement (MSAD) $\langle\Delta\theta(\Delta r)^2\rangle$ normalized by the short-time rotational diffusion coefficient D_s^{rot} and **(B)** orientation correlation function $\langle\cos(\Delta\theta(\Delta r))\rangle$ as a function of displacement Δr normalized by the sphere diameter σ for trimers exposed to different laser intensities P_L (as indicated).

particle traveled. At very small distances and hence without significant translation, rotations can occur. In contrast, rotations are coupled to translations at intermediate distances ($0.8\,\mu\text{m} \leq \Delta r \leq 1.4\,\mu\text{m}$). At larger distances translations and rotations are again decoupled.

In addition to the maxima of the van Hove function $G_s(\Delta\theta, \Delta r)$, the general broadening of $G_s(\Delta\theta, \Delta r)$ is characterized by the mean squared angular displacement (MSAD) $\langle\Delta\theta^2(\Delta r)\rangle$ as a function of the translational displacement Δr (**Figure 14A**). Without an external potential, $\langle\Delta\theta^2(\Delta r)\rangle$ increases with increasing translational displacement Δr. In contrast to $\langle\Delta\theta^2(\tau)\rangle$ (**Figure 7A**), $\langle\Delta\theta^2(\Delta r)\rangle$ starts at $\Delta r = 0$ with a finite value since the trimer can rotate without translating, whereas it cannot rotate in no time ($\langle\Delta\theta^2(\tau{=}0)\rangle = 0$). In the presence of an external potential, translation is restricted and hence even larger angular displacements are possible during small translational displacements. With increasing translational displacements, $\langle\Delta\theta^2(\Delta r)\rangle$ increases further.

The experimental uncertainties at large displacements are quite considerable in the presence of a random potential. This is due to the long time required for large displacements resulting in only a small number of large displacements being observed. This is particularly true for large laser intensities P_L. The data shown in **Figure 14** are based on at least 150 displacements. This number of displacements is easily observed without an external potential. However, with increasing laser intensity P_L, this number of displacements is only detected for progressively smaller displacements Δr. Nevertheless, within the experimental uncertainties, the data suggest that $\langle\Delta\theta^2(\Delta r)\rangle$ does not depend on the laser intensity P_L. This implies that the random potential slows down the translation and rotation of the trimers equally. This seems reasonable because the spheres have to move in the same random potential for both, a translation and a rotation of the trimer. Translation and rotation are considered separately only to simplify the analysis and data interpretation and thus for our convenience. Moreover, although at large distances Δr the uncertainties do not allow for unambiguous conclusions, the data seem to indicate that $\langle\Delta\theta^2(\Delta r)\rangle$ might not depend on the presence of an external potential at distances beyond

$\Delta r \approx 2\,\mu$m. This is about the spatial correlation length of the random potential [34]. This suggests that, at distances larger than the spatial heterogeneity of the random potential, the random potential has no specific effect on the translation and rotation except to generally slow down the motion. In contrast, at distances smaller than the spatial heterogeneity, the random potential leads to specific movements resulting in all or some of the occupied minima remaining occupied (**Figure 13**).

The coupling between rotation and translation is also characterized by the orientation correlation function $\langle \cos(\Delta\theta(\Delta r))\rangle$ (**Figure 14B**). Essentially independent of the laser intensity P_L, the orientation correlation function $\langle \cos(\Delta\theta(\Delta r))\rangle$ decays within $\Delta r \approx 2\,\mu$m and hence on a length scale very similar to the one found above and to the spatial correlation length of the random potential [34]. Additionally, $\langle \cos(\Delta\theta(\Delta r))\rangle$ for trimers not exposed to a random potential decays on a comparable length scale. This could be a coincidence since the spatial correlation length of the random potential and the size of an individual sphere are similar. Future experiments with different particle sizes and different spatial correlation lengths, which can be varied as previously described [34], will be devoted to this issue.

4. CONCLUSIONS

The translational and rotational dynamics of trimers subjected to a random potential energy landscape have been investigated. The translational center-of-mass motion is characterized by subdiffusion at intermediate times due to the confinement to the minima and diffusion at long times reflecting the random motion between minima. The dynamics hence resemble the dynamics of spheres, which are the building blocks of the trimers, but the trimers are more strongly affected by the potential. The rotational mean squared angular displacements (MSAD) are only slightly affected by the potential. However, a more detailed analysis based on the van Hove distribution function and the hop identifier indicates discrete jumps of 120° that are particularly pronounced at long times and large magnitudes of the modulations of the random potential. These jumps are found to dominate the long-time rotational diffusion.

The rotational motion is correlated with the translational motion due to the symmetry of the trimers. During the angular jumps of about 120°, the spheres forming the trimer swap their positions without any significant translational motion. If only two out of the three initial minima remain occupied, a jump of 60° is coupled to a translational motion between $\sim$ 0.8 and 1.4 μm. This is in agreement with an idealized model (**Figure 13**). Upon a larger translational motion, beyond the spatial correlation length of the random potential, any angular displacement becomes possible and hence the correlation between translation and rotation is lost. In this regime, the random potential slows down the translational and rotational dynamics equally.

The work presented here can be extended in future projects. For example, different particle or speckle sizes could be investigated to study the effect of their size ratio. Depending on the size ratio, the rotational dynamics could be favored or disfavoured compared to the translational dynamics. The coupling between translation and rotation might also be affected by the symmetry of the particles and hence other multimers, such as dumbbells, or other anisotropic particles, such as elliptical or platelike particles, could be studied. In addition, in concentrated samples the interplay between the external random potential and the particle–particle interactions can be explored. The random potential could also be replaced by a periodic potential which would also have a very significant effect on the correlation between translation and rotation.

DATA AVAILABILITY STATEMENT

The datasets generated for this study are available on request to the corresponding author.

AUTHOR CONTRIBUTIONS

JS-G, ME-S, and SE designed the experiments. JS-G and ME-S prepared the particles. JS-G performed the experiments. JS-G, ME-S, ES-G, and SE analyzed the data. JS-G, ES-G, and SE wrote the manuscript.

FUNDING

This work was supported by the Deutsche Forschungsgemeinschaft (DFG), Project No. EG269/6-1.

ACKNOWLEDGMENTS

We thank Daniela Pérez-Guerrero, Milana Popara, and Alejandro Villada-Balbuena for useful discussions and for early contributions to the project and Katherine Macmillan for very helpful comments on the manuscript as well as the referees for very helpful and inspiring comments.

REFERENCES

1. Metzler R, Jeon JH, Cherstvy AG, Barkai E. Anomalous diffusion models and their properties: non-stationarity, non-ergodicity, and ageing at the centenary of single particle tracking. *Phys Chem Chem Phys.* (2014) **16**:24128–64. doi: 10.1039/C4CP03465A
2. Weiss M, Elsner M, Kartberg F, Nilsson T. Anomalous subdiffusion is a measure for cytoplasmic crowding in living cells. *Biophys J.* (2004) **87**:3518–24. doi: 10.1529/biophysj.104.044263
3. Seisenberger G, Ried MU, Endress T, Büning H, Hallek M, Bräuchle C. Real-time single-molecule imaging of the infection pathway of an adeno-associated virus. *Science.* (2001) **294**:1929–32. doi: 10.1126/science.1064103
4. Reverey JF, Jeon JH, Bao H, Leippe M, Metzler R, Selhuber-Unkel C. Superdiffusion dominates intracellular particle motion in the supercrowded cytoplasm of pathogenic *Acanthamoeba castellanii*. *Sci Rep.* (2015) **5**:11690. doi: 10.1038/srep11690
5. Thapa S, Lukat N, Selhuber-Unke C, Cherstvy AG, Metzler R. Transient superdiffusion of polydisperse vacuoles in highly motile

amoeboid cells. *J Chem Phys.* (2019) **150**:144901. doi: 10.1063/1.5086269
6. Nicolau DV, Hancock JF, Burrage K. Sources of anomalous diffusion on cell membranes: a Monte Carlo study. *Biophys J.* (2007) **92**:1975–87. doi: 10.1529/biophysj.105.076869
7. Metzler R, Jeon JH, Cherstvy AG. Non-Brownian diffusion in lipid membranes: Experiments and simulations. *Biochim Biophys Acta.* (2016) **1858**:2451–67. doi: 10.1016/j.bbamem.2016.01.022
8. Daddi-Moussa-Ider A, Goh S, Liebchen B, Hoell C, Mathijssen AJTM, Guzmán-Lastra F, et al. Membrane penetration and trappingof an active particle. *J Chem Phys.* (2019) **150**:064906. doi: 10.1063/1.5080807
9. Dickson RM, Norris DJ, Tzeng Y, Moerner WE. Three-dimensional imaging of single molecules solvated in pores of poly(acrylamide) gels. *Science.* (1996) **274**:966–8. doi: 10.1126/science.274.5289.966
10. Gibbs JH, DiMarzio EA. Nature of the glass transition and the glassy state. *J Chem Phys.* (1958) **28**:373–83. doi: 10.1063/1.1744141
11. Adam G, Gibbs JH. On the temperature dependence of cooperative relaxation properties in glass-forming liquids. *J Chem Phys.* (1965) **43**:139–46. doi: 10.1063/1.1696442
12. Heuer A. Exploring the potential energy landscape of glass-forming systems: from inherent structures via metabasins to macroscopic transport. *J Phys Condens Matter.* (2008) **20**:373101. doi: 10.1088/0953-8984/20/37/373101
13. Hunter GL, Weeks ER. The physics of the colloidal glass transition. *Rep Prog Phys.* (2012) **75**:066501. doi: 10.1088/0034-4885/75/6/066501
14. Stillinger FH, Debenedetti PG. Glass transition thermodynamics and kinetics. *Annu Rev Condens Matter Phys.* (2013) **4**:263–85. doi: 10.1146/annurev-conmatphys-030212-184329
15. Ho CC, Keller A, Odell JA, Ottewill RH. Preparation of monodisperse ellipsoidal polystyrene particles. *Coll Polym Sci.* (1993) **271**:469–79. doi: 10.1007/BF00657391
16. Wolters JR, Avvisati G, Hagemans F, Vissers T, Kraft DJ, Dijkstra M, et al. Self-assembly of "Mickey Mouse" shaped colloids into tube-like structures: experiments and simulations. *Soft Matter.* (2015) **11**:1067–77. doi: 10.1039/C4SM02375G
17. Peng B, van der Wee E, Imhof A, van Blaaderen A. Synthesis of monodisperse, highly Cross-Linked, fluorescent PMMA particles by dispersion polymerization. *Langmuir.* (2012) **28**:6776–85. doi: 10.1021/la301288r
18. Manoharan VN, Elsesser MT, Pine DJ. Dense packing and symmetry in small clusters of microspheres. *Science.* (2003) **301**:483. doi: 10.1126/science.1086189
19. Han Y, Alsayed AM, Nobili M, Zhang J, Lubensky TC, Yodh AG. Brownian motion of an ellipsoid. *Science.* (2006) **314**:626–30. doi: 10.1126/science.1130146
20. Villanueva-Valencia JR, Santana-Solano J, Sarmiento-Gómez E, Herrera-Velarde S, Arauz-Lara JL, Castaneda-Priego R. Long-time dynamics and hydrodynamic correlations in quasi-two-dimensional anisotropic colloidal mixtures. *Phys Rev E.* (2018) **98**:062605. doi: 10.1103/PhysRevE.98.062605
21. Vivek S, Weeks ER. Decoupling of translational and rotational diffusion in quasi-2D colloidal fluids. *J Chem Phys.* (2017) **147**:134502. doi: 10.1063/1.4996733
22. Anthony SM, Kim M, Granick S. Translation-rotation decoupling of colloidal clusters of various symmetries. *J Chem Phys.* (2008) **129**:244701. doi: 10.1063/1.3043443
23. Edmond KV, Elsesser MT, Hunter GL, Pine DJ, Weeks ER. Decoupling of rotational and translational diffusion in supercooled colloidal fluids. *Proc Natl Acad Sci USA.* (2012) **109**:17891–6. doi: 10.1073/pnas.1203328109
24. Jeon H, Cho HW, Kim J, Sung BJ. Non-Gaussian rotational diffusion in heterogeneous media. *Phys Rev E.* (2014) **90**:042105. doi: 10.1103/PhysRevE.90.042105
25. Ashkin A. Acceleration and trapping of particles by radiation pressure. *Phys Rev Lett.* (1970) **24**:156–9. doi: 10.1103/PhysRevLett.24.156
26. Ashkin A, Dziedzic JM, Bjorkholm JE, Chu S. Observation of a single-beam gradient force optical trap for dielectric particles. *Opt Lett.* (1986) **11**:288–90. doi: 10.1364/OL.11.000288
27. Molloy JE, Padgett MJ. Lights, action: optical tweezers. *Contemp Phys.* (2002) **43**:241–58. doi: 10.1080/00107510110116051
28. Neuman KC, Block SM. Optical trapping. *Rev Sci Instrum.* (2004) **75**:2787–809. doi: 10.1063/1.1785844
29. Dienerowitz M, Mazilu M, Dholakia K. Optical manipulation of nanoparticles: a reivew. *J Nanophoton.* (2008) **2**:021875. doi: 10.1117/1.2992045
30. Evers F, Hanes RDL, Zunke C, Capellmann RF, Bewerunge J, Dalle-Ferrier C, et al. Colloids in light fields: Particle dynamics in random and periodic energy landscapes. *Eur Phys J Special Topics.* (2013) **222**:2995–3009. doi: 10.1140/epjst/e2013-02071-2
31. Jenkins MC, Egelhaaf SU. Colloidal suspensions in modulated light fields. *J Phys Condens Matter.* (2008) **20**:404220. doi: 10.1088/0953-8984/20/40/404220
32. Capellmann RF, Bewerunge J, Platten F, Egelhaaf SU. Note: using a Kösters prism to create a fringe pattern. *Rev Sci Instrum.* (2017) **88**:056102. doi: 10.1063/1.4982587
33. Juniper MPN, Besseling R, Aarts DGAL, Dullens RPA. Acousto-optically generated potential energy landscapes: Potential mapping using colloids under flow. *Opt Express.* (2012) **20**:28707–16. doi: 10.1364/OE.20.028707
34. Bewerunge J, Egelhaaf SU. Experimental creation and characterization of random potential-energy landscapes exploiting speckle patterns. *Phys Rev A.* (2016) **93**:013806. doi: 10.1103/PhysRevA.93.013806
35. Hanes RDL, Jenkins MC, Egelhaaf SU. Combined holographic-mechanical optical tweezers: construction, optimization, and calibration. *Rev Sci Instrum.* (2009) **80**:083703. doi: 10.1063/1.3196181
36. Abbott JL, Spiers JA, Gao Y, Aarts DGA, Dullens RPA. Colloidal rods in optical potential energy landscapes. *J Phys D Appl Phys.* (2019) **52**:024002. doi: 10.1088/1361-6463/aae5d0
37. Dalle-Ferrier C, Krüger M, Hanes RDL, Walta S, Jenkins MC, Egelhaaf SU. Dynamics of dilute colloidal suspensions in modulated potentials. *Soft Matter.* (2011) **7**:2064–75. doi: 10.1039/C0SM01051K
38. Hanes RDL, Dalle-Ferrier C, Schmiedeberg M, Jenkins MC, Egelhaaf SU. Colloids in one dimensional random energy landscapes. *Soft Matter.* (2012) **8**:2714–23. doi: 10.1039/c2sm07102a
39. Evers F, Zunke C, Hanes RDL, Bewerunge J, Ladadwa I, Heuer A, et al. Particle dynamics in two-dimensional random-energy landscapes: Experiments and simulations. *Phys Rev E.* (2013) **88**:022125. doi: 10.1103/PhysRevE.88.022125
40. Bianchi S, Pruner R, Vizsnyiczai G, Maggi C, Leonardo RD. Active dynamics of colloidal particles in time-varying laser speckle patterns. *Sci Rep.* (2016) **6**:27681. doi: 10.1038/srep27681
41. Volpe G, Volpe G, Gigan S. Brownian motion in a speckle light field: tunable anomalous diffusion and selective optical manipulation. *Sci Rep.* (2014) **4**:3936. doi: 10.1038/srep03936
42. Sarmiento-Gómez E, Rivera-Morána JA, Arauz-Lara JL. Single particle states of colloidal particles in 2D periodic potentials. *Soft Matter.* (2018) **14**:3684–8. doi: 10.1039/C8SM00326B
43. Sarmiento-Gómez E, Rivera-Morána JA, Arauz-Lara JL. Energy landscape of colloidal dumbbells in a periodic distribution of light. *Soft Matter.* (2019) **15**:3573–9. doi: 10.1039/C9SM00472F
44. Dullens RPA, Claesson EM, Kegel WK. Preparation and properties of cross-linked fluorescent poly(methyl methacrylate) latex colloids. *Langmuir.* (2004) **20**:658–64. doi: 10.1021/la035729a
45. Elsesser MT, Hollingsworth AD, Edmond KV, Pine DJ. Large core-shell poly(methyl methacrylate) colloidal clusters: synthesis, characterization, and tracking. *Langmuir.* (2010) **27**:917–27. doi: 10.1021/la1034905
46. Antl L, Goodwin JW, Hill RD, Ottewill RH, Owens SM, Papworth S. The preparation of poly(methyl methacrylate) lattices in non-aqueous media. *Coll Surf.* (1986) **17**:67–78. doi: 10.1016/0166-6622(86)80187-1
47. Carbajal-Tinoco MD, de Léon GC, Arauz-Lara JL. Brownian motion in quasibidimensional colloidal suspensions. *Phys Rev E.* (1997) **56**:6962. doi: 10.1103/PhysRevE.56.6962
48. Crocker JC, Grier DG. Methods of digital video microscopy for colloidal studies. *J Coll Interf Sci.* (1996) **179**:298–310. doi: 10.1006/jcis.1996.0217
49. Landau LD, Lifshitz EM. *The Cassical Theory of Fields.* London: Pergamon Press (1971).
50. Dean DS, Drummond IT, Horgan RR. Effective transport properties for diffusion in random media. *J Stat Mech.* (2007) **2007**:P07013. doi: 10.1088/1742-5468/2007/07/P07013
51. Bewerunge J, Ladadwa I, Platten F, Zunke C, Heuer A, Egelhaaf SU. Time- and ensemble-averages in evolving systems: the case of Brownian particles in random potentials. *Phys Chem Chem Phys.* (2016) **18**:18887–95. doi: 10.1039/C6CP02559E

52. Pagac ES, Tilton RD, Prieve DC. Hindered mobility of a rigid sphere near a wall. *Chem Eng Comm.* (1996) **148–50**:105–22. doi: 10.1080/00986449608936511
53. Sharma P, Ghosh S, Bhattacharya S. A high-precision study of hindered diffusion near a wall. *Appl Phys Lett.* (2010) **97**:104101. doi: 10.1063/1.3486123
54. Rahman A. Correlations in the motion of atoms in liquid argon. *Phys Rev.* (1964) **136**:A405. doi: 10.1103/PhysRev.136.A405
55. Shell MS, Debenedetti PG, Stillinger FH. Dynamic heterogeneity and non-Gaussian behaviour in a model supercooled liquid. *J Phys Condens Matter.* (2005) **17**:S4035–46. doi: 10.1088/0953-8984/17/49/002
56. Vorselaars B, Lyulin AV, Karatasos K, Michels MAJ. Non-Gaussian nature of glassy dynamics by cage to cage motion. *Soft Matter.* (2007) **75**:011504. doi: 10.1103/PhysRevE.75.011504
57. Candelier R, Widmer-Cooper A, Kummerfeld JK, Dauchot O, Biroli G, Harrowell P, et al. Spatiotemporal hierarchy of relaxation events, dynamical heterogeneities, and structural reorganization in a supercooled liquid. *Phys Rev Lett.* (2010) **105**:135702. doi: 10.1103/PhysRevLett.105.135702
58. Smessaert A, Rottler J. Distribution of local relaxation events in an aging three-dimensional glass: spatiotemporal correlation and dynamical heterogeneity. *Phys Rev E.* (2013) **88**:022314. doi: 10.1103/PhysRevE.88.022314

Conflict of Interest: The authors declare that the research was conducted in the absence of any commercial or financial relationships that could be construed as a potential conflict of interest.